Separating and Quantifying Facility-Level Methane Emissions with Overlapping Plumes for Spaceborne Methane Monitoring

Yiguo Pang[1,2], Longfei Tian[1], Denghui Hu[1], Shuang Gao[1], and Guohua Liu[1,2]

[1]Innovation Academy for Microsatellites of Chinese Academy of Sciences, Shanghai China.
[2]University of Chinese Academy of Sciences, Beijing, China.

Correspondence: Guohua Liu (liugh@microsate.com)

Abstract.

Quantifying facility-level methane emission rates using satellites with fine spatial resolution has recently gained significant attention. However, the prevailing quantification algorithms usually require the methane column plume from a solitary point source as input. Such approaches are challenged with overlapping plumes from multiple point sources. To address these challenges, we propose a separation approach based on a heuristic optimization and the multi-source Gaussian plume model to separate the overlapping plumes. Subsequently, the integrated mass enhancement (IME) model is applied to accurately quantify emission rates. To validate the proposed method, observation system simulation experiments (OSSE) of various scenarios are performed. The result shows that plume overlapping exacerbates the quantifying error of the IME method when applied without such separation approach, where the quantification mean absolute percentage error (MAPE) increased from 0.15 to 0.83, and it is affected by factors such as source intervals, wind direction, and interference emission rates. By contrast, the application of the proposed separation method together with the IME quantification approach mitigates this interference, reducing the quantification MAPE from 0.83 to 0.38. Moreover, the proposed method also outperforms the direct use of multi-source Gaussian plume fitting for the quantification, with a MAPE of 0.45. Our separation method separates overlapping plumes from multiple sources into distinct, single-source observations, enabling the IME algorithm—a high-precision quantification approach for fine spatial resolution plume images—to handle multi-source scenarios effectively. This method can help future spaceborne carbon inventorying on spatially clustering carbon-emitting facilities.

1 Introduction

Since the industrial revolution, the increasing anthropogenic emissions of greenhouse gases (GHG), have emerged as the foremost contributor to global warming and climate change, obstructing global sustainable development (IPCC, 2021). To tackle this challenge, the global community has united and expressed a strong will to limit long-term warming below 1.5°C above the pre-industrial level, as stipulated in the Paris Agreement under the United Nations Framework Convention on Climate Change (UNFCCC). Comprehensive monitoring of global GHG is vital for verifying human activities' impacts on climate change, observing climate change trends, formulating solutions to address climate change, and evaluating the efficacy of climate policies. The conventional way to estimate GHG emissions is to multiply the elements of human activities by emission

factors, using statistical methods (Calvo Buendia et al., 2019). Yet, owing to the substantial uncertainty of emission factors and source coverage (Zhao et al., 2017; Suarez et al., 2019), the performance of this bottom-up method is limited. In this regard, spaceborne GHG monitoring capabilities, e.g., OCO-2/3 (Nassar et al., 2017), TROPOMI (Zhang et al., 2020) and TanSat (Yang et al., 2023), have demonstrated their ability to quantify anthropogenic GHG emissions from large sources, such as cities and large thermal power plants, which are considered point sources. Spaceborne GHG monitoring is capable of undertaking independent, objective, and high spatiotemporal coverage measuring, and is thus considered important to verify the accuracy of bottom-up GHG emission inventories (Calvo Buendia et al., 2019; Liu et al., 2022).

Methane (CH_4) is a greenhouse gas second only to carbon dioxide(CO_2) in terms of radiative forcing, with a global warming potential (GWP-100) of about 27-29 times that of CO_2 on unit emission and a lifespan of only about 11.8 years (IPCC, 2021). As a result, taking proactive measures to reduce anthropogenic methane emissions can help alleviate global warming in the short term. Numerous studies indicate that anthropogenic methane emissions are primarily concentrated at a number of high-emission point sources (Nisbet et al., 2020; Cusworth et al., 2020; Duren et al., 2019; Frankenberg et al., 2016). Furthermore, a detected methane plume typically shows a higher signal-to-noise ratio (SNR) than CO_2 due to the significantly lower background concentration of methane (around 1.8 ppm) compared to CO_2 (approximately 420 ppm), as well as the stronger absorption cross-section of methane. These features provide convenience for spaceborne monitoring of anthropogenic methane emissions. A recent trend is monitoring methane point sources using orbital instruments with fine spatial resolution, as smaller pixels are more sensitive to column enhancement of point sources with relatively lower emissions rates (Jervis et al., 2021).For instance, GHGSat is a dedicated commercial constellation for GHG point source monitoring, with a resolution of 25–50 m (Jervis et al., 2021). Its supper fine spectral resolution endows it with a low retrieval uncertainty of 1-5% (Varon et al., 2018). Guanter et al. (2021) described detecting methane plumes with PRISMA, a versatile hyperspectral satellite. Sánchez-García et al. (2022) elucidated the detection of methane plumes with WorldView-3, a commercial multispectral satellite with a spatial resolution of 3.5 m.

One of the primary purposes of spaceborne methane point source monitoring is to quantify the emission rates. To do so, a widely used method is spaceborne measuring backscattered solar radiation in visible and shortwave infrared (VSWIR). The methane concentration (or its enhancement) is then retrieved using inversion algorithms, such as the optimal estimation based methods (Rodgers, 2000; Frankenberg et al., 2005; Jervis et al., 2021); data driven methods, such as matched filter (Thorpe et al., 2014) and deep learning methods (Özdemir and Koz, 2023). The emission rates of methane point sources are then estimated using quantification methods, which can be broadly divided into two categories. The first category generally allows for direct quantification, such as Gaussian plume fitting (Bovensmann et al., 2010; Nassar et al., 2017, 2021). The second category often requires clear detection of plume pixels from the observation, such as integrated mass enhancement (IME; Frankenberg et al., 2016; Varon et al., 2018) method. To detect the plume pixels, Nassar et al. (2017) distinct the plume and the backgrounds with a 1 % density cutoff criteria; Kuhlmann et al. (2019) proposes a Z-test based plume detection algorithm to mask pixels with statistically higher values; Varon et al. (2018) combines Student's t-test with computer vision (CV) based methods to detect plume pixels; Joyce et al. (2023) uses deep learning method for the detection.

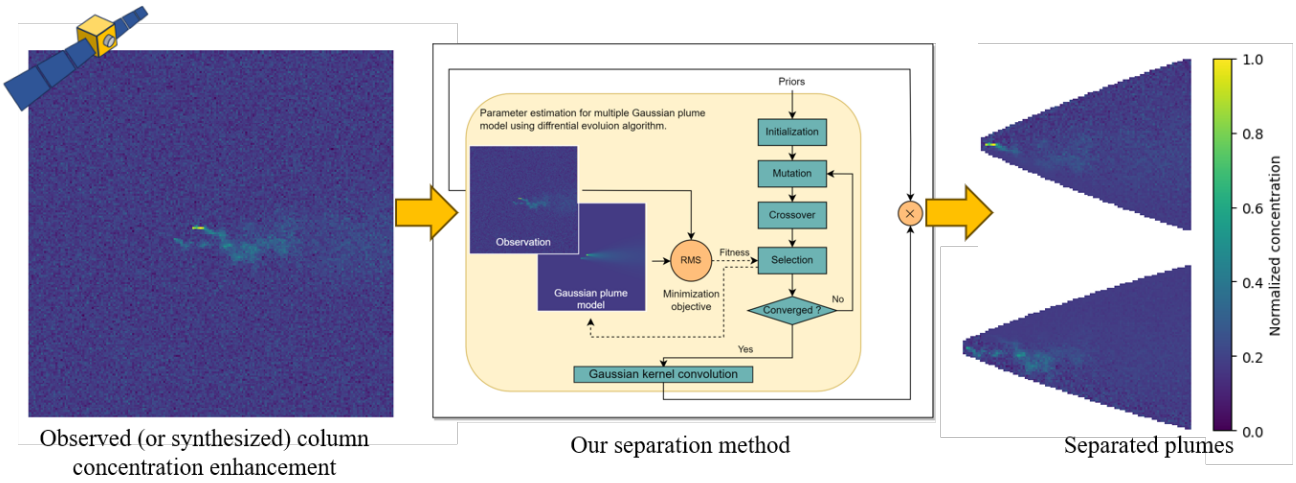

Figure 1. The proposed methodology for separating overlapping plumes. A heuristic optimization-based method is proposed to estimate the Gaussian plume parameters for each source to separate the overlapping plumes. This method utilizes observed methane column enhancement and auxiliary data with uncertainty as inputs, yielding the enhancements of separated plumes. The separated plumes are then quantified with the more precise IME method respectively.

However, limited research has specifically addressed the quantification of methane emissions originating from overlapping plumes emitted by multiple spatially adjacent sources. Plume overlapping can be not uncommon. Based on the analysis of the VISTA-CA inventory (Hopkins et al., 2019) of potential methane sources in California, US, it is found that >90% of the intervals of a source to its neighbor are less than 200 m. Upon excluding the "oil and gas well", constituting 96.5% of the total, the median and mean intervals become 496 m and 1247 m, respectively, indicating a spatial clustering distribution trend, potentially resulting in overlapping plumes. Plume overlapping poses a challenge to quantification as it breaks the one-to-one correspondence between a plume pixel and a source, which means the mass in each detected plume pixel may originate from multiple sources, introducing additional errors in quantification when the mass in a conjoint pixel is attributed to any single source. Several studies have encountered the challenge of plume overlapping, which significantly complicates the quantification process (Kuhlmann et al., 2019) and, in extreme cases, makes quantification impossible (Duren et al., 2019; Kuhlmann et al., 2020; Sánchez-García et al., 2022).Therefore, it is necessary to separate the overlapping plumes and to establish one-to-one correspondences between plume pixels and emission sources, thus enabling accurate inventorying of emission rates for each individual source.

There have been several studies using Gaussian plume fitting to solve plume overlapping problems for spaceborne GHG monitoring. For example, Krings et al. (2011) employed a Gauss-Newton iteration-based optimal estimation approach to infer the emission rates of sources with overlapping plumes; Nassar et al. (2017, 2021) employed a method of Gaussian plume combinations, where the interference sources are fixed, reducing the multi-source estimation problem into a single-source estimation problem. These methods can handle the plume overlapping on a large scale. However, these methods are challenged

for facility-level monitoring, where the auxiliary information is inaccurate or even unknown. Moreover, the Gaussian plume demonstrates uncertainty with small-scale plumes (Varon et al., 2018).

To address these challenges, we propose an approach to derive emission rates from overlapping plumes through separation and quantification. This approach is composed with a Gaussian plume weighting separation method (shown in Fig. 1) for plume separation and the traditional IME method for quantification. Firstly, the Gaussian plume weighting is based on parameter estimation for the multi-source Gaussian plume model. To mitigate the effects of inaccurate or missing auxiliary data, we introduce the optimization algorithm to perform parameter estimation. This approach is inspired by Allen et al. (2007) and Haupt et al. (2007), who utilize the genetic algorithm, a subclass of heuristic optimization algorithms, to infer pollutant emission rates by estimating Gaussian plume parameters, such as source emission rate, source location and surface wind direction, using ground-based sensors. Secondly, to address the limited performance of direct quantification from Gaussian plume fitting at fine resolution, we employ the IME method for more precise quantification after the separation.

To study the impact of overlapping and the performance of various quantification method, we simulate plumes using large eddy simulations conducted by the Weather and Research Forecasting Model (WRF-LES; https://www.mmm.ucar.edu/models/wrf). Subsequently, we synthesize observations of various sources, meteorological conditions, and observation characteristics based on these simulated plumes. The synthesized observations comprised three scenarios of Observation System Simulation Experiments (OSSE), including single-source, dual-source, and real scenarios. Within these experiments, we compare the performance of the proposed method in quantification errors against conventional methods (shown in Table 1), including single source Gaussian plume method, multi-source Gaussian plume method, and IME method without separation. Furthermore, we validate our method by applying it to a genuine satellite-observed case featuring overlapping plumes.

2 Methods

2.1 Separation and quantification method for overlapping plumes of multiple sources

In this section, a separation and quantification approach is proposed to quantify facility-level methane emissions with overlapping plumes. As shown in Table 1, the proposed method is composed of a Gaussian plume weighting separation process, the plume detection process and IME quantification process. The Section 2.1.1 describes the formulation of the Gaussian plume models. Section 2.1.2 describes parameter estimation for the Gaussian plume models using heuristic optimization algorithm. Section 2.1.3 describes the Gaussian plume weighting separation. Section 2.1.4 describes the detection method and the IME quantification method.

Section 2.1.4 describes the combination of the separation method and the IME method for the quantification.

2.1.1 2-D Gaussian plume model

The transport mechanism of methane from point sources in the atmospheric boundary layer (ABL) can be very complicated, as affected by multiple factors such as atmospheric turbulence, chemical reactions and terrain effects. From the perspective

Table 1. Comparison of methods evaluated in this work.

Method	Separation	Detection	Quantification
Single-source Gaussian plume	/	Single-source Gaussian plume fitting	
Multi-source Gaussian plume	Multi-source Gaussian plume fitting		
UNSEP	/	Student's t-test & Connectivity filtering	IME method
SEP (ours)	Gaussian plume weighting separation	Student's t-test & Connectivity filtering	IME method

of mass conservation, considering wind transport, gradient diffusion, and source-sink terms, the convection-diffusion equation can be obtained to represent this mechanism, which can be written as (Stockie, 2011)

$$\frac{\partial C}{\partial t} + \nabla \cdot (C\boldsymbol{u}) = \nabla \cdot (\mathbf{K}\nabla C) + S, \tag{1}$$

where C represents the methane column mass concentration at a certain moment; t represents time; $\boldsymbol{u}$ represents the 2D field of wind velocity vectors; matrix $\mathbf{K}$ is diagonal, with its elements representing diffusion coefficients for each wind velocity direction; S represents the source item.

One way to solve this partial differential equation (PDE) is the numerical method (e.g., Hosseini and Stockie, 2017). However, the computational cost can be enormous. Analytical methods, on the other hand, simplify the problem by making assumptions, allowing for the derivation of analytical solutions to the PDE. For instance, the Gaussian plume expression of a point source can be obtained from the convection-diffusion equation by assuming that the wind speed is constant and uniform, the emission rate is time-invariant and the turbulence is negligible (Sutton, 1932; Ermak, 1977; Stockie, 2011). The Gaussian plume model is widely applied to describe the pollutants, as well as the GHG dispersion in ABL, particularly in spaceborne GHG monitoring research (Bovensmann et al., 2010; Nassar et al., 2021; Jacob et al., 2022). As a result, we model the column mass concentration(kg m^{-2}) at the location (x, y) using a 2D Gaussian plume model for a ground-level point source, which can be written as (Sutton, 1932; Bovensmann et al., 2010)

$$C_{\mathrm{SGP}}(x, y; Q, u) = \frac{Q}{\sqrt{2\pi}\sigma_y(x)u} \exp(-\frac{1}{2}(\frac{y}{\sigma_y(x)})^2), \tag{2}$$

where the x-axis is aligned with the direction of wind speed; Q represents the emission rate (kg s^{-1}); u represents the horizontal wind speed (m s^{-1}) at the plume height; σ_y represents the diffusion coefficient across-wind, which is a function of downwind distance x and is decided by wind speed, underlying condition and sunlight (Briggs, 1973). Eq.2 then can be extended to multiple source scenarios of N sources and the corresponding concentration is given by

$$C_{\mathrm{MGP}}(x, y) = \sum_{n=1}^{N} C_{\mathrm{SGP}}(x'_n, y'_n; Q_n, u_n), \tag{3}$$

where

$$\begin{bmatrix} x'_n \\ y'_n \end{bmatrix} = \begin{bmatrix} \cos\theta_n & \sin\theta_n \\ -\sin\theta_n & \cos\theta_n \end{bmatrix} \begin{bmatrix} x - x_n \\ y - y_n \end{bmatrix}. \tag{4}$$

Here Q_n and u_n denotes the emission rate and wind speed of point source n at coordinates (x_n, y_n), respectively; θ_n represents the wind speed angle of source n in an easting/northing Cartesian coordinate system, where 0° and 90° represent the eastward and northward winds, respectively. We presume uniform wind conditions for the modeled plumes (i.e., $u_n = u, \theta_n = \theta, \forall n \in 1, 2, ..., N$) in this work, given the spatially limited extent of facility-level plumes. This method simplifies subsequent parameter estimation to improve the convergence.

2.1.2 Gaussian plume fitting using heuristic optimization algorithm

A heuristic optimization algorithm is introduced for parameter estimation of the Gaussian plume model discussed in Section 2.1.1. Heuristics optimization algorithms are capable of global searching in optimization and are thus widely used for solving optimization problems. Heuristics optimization algorithms have been widely used in parameter estimation of point source dispersion models (Hutchinson et al., 2017), e.g., Allen et al. (2007), Haupt et al. (2007) and Cervone et al. (2010), showing more robust performance compared to other optimization methods such as Bayesian inference (Platt and DeRiggi, 2012). The differential evolution algorithm (Storn and Price, 1997) is a heuristic optimization algorithm inspired by the evolution theory of biological species.

In this study, the differential evolution algorithm is selected as the estimation algorithm to iteratively minimize the metrics between the modeled concentration image by Eq.3 and the observed concentration image, to estimate the parameters of the dispersion model.

Here, the estimating parameters consist of source locations (x_i, y_i) and emission rates Q_i of source i, the global wind angle θ and wind velocity u. For the application of the differential evolution algorithm in this paper, the searching spaces for the estimating parameters are set as follows: $\pm$ 100 m for source locations (x_i, y_i) from their true values; $\pm$ 50% for the wind velocity from its true value, higher than the average errors of the widely used reanalysis meteorological database analyzed by Varon et al. (2018) and Duren et al. (2019); $\pm$ 45° for the wind angle θ from its true value; $0 - 5000$ kg h^{-1} for emission rates Q_i, covering all methane point sources in Duren et al. (2019).

The minimization objective is another important part to apply the optimization algorithm. The most widely used minimization objective is to minimize the root mean square (RMS) metrics between modeled and observed concentration images. The RMS metric is given as

$$\mathcal{L}_{\mathrm{RMS}} = \sqrt{\sum_{i,j} \Big(I_{\mathrm{model}}(i,j) - I_{\mathrm{obs}}(i,j) \Big)^2}, \tag{5}$$

where $I_{\mathrm{model}}(i,j)$ and $I_{\mathrm{obs}}(i,j)$ represent the modeled and observed concentration images, respectively; i and j represent the pixel indexes in row and column, respectively.

In the application of the differential evolution algorithm, the mutation strategy is set as best-guided mutation, i.e., DE2 in Storn and Price (1997); the number of population (NP) is set as $10 \times (N \times 3 + 2)$, where N represents the number of sources; 3 and 2 represent the numbers of parameters to be estimated for each source and entire observation, respectively; The mutation constant (F) is set as 1 and the cross-over constant (CR) is set as 0.9 according to Storn and Price (1997); the relative convergence criteria is set as 10^{-3}.

2.1.3 Gaussian plume weighting separation

Fig. 1 illustrates the framework to separate an image of overlapping plumes into distinct images, each with a solitary plume. The parameters of the Gaussian plume model are estimated iteratively using the heuristic optimization algorithm described in Section 2.1.2, generating a series of images each with its corresponding modeled Gaussian plume. These Gaussian plumes are then utilized as weights to allocate the original observation image pixel by pixel. However, due to the stochastic nature of the transient plume at such small scales, there can be slight misalignments between the modeled Gaussian plume and the transient plume, particularly near the source, which brings obstacles to the following allocation. To address this misalignment issue, we employ Gaussian blur (i.e., convolution with a 2D Gaussian kernel) to smooth the modeled plumes, thereby increasing robustness against the deviations of the transient plume. Formally, an image with separated plume $\hat{I}_{\mathrm{obs},n}$ of source n from observation I_{obs} is given by

$$\hat{I}_{\mathrm{obs},n} = I_{\mathrm{obs}} \cdot \frac{< C_{\mathrm{SGP},n} >}{\sum_{p=1}^{N} < C_{\mathrm{SGP},p} >}, \tag{6}$$

where $C_{\mathrm{SGP},n}, C_{\mathrm{SGP},p}$ represents the modeled Gaussian plume image of source n and p, respectively; $< \cdot >$ represents the Gaussian blur operation.

2.1.4 Plume detection and IME quantification

A transient plume may exhibit significant deviations from the Gaussian plume at small scales, leading to unstable quantification with Gaussian plume fitting. In contrast, the integrated mass enhancement (IME) method demonstrate better accuracy in qunatifying small-scale transient plumes (Varon et al., 2018; Jongaramrungruang et al., 2019). Therefore, we employ the IME method for more precise quantification on the separated plumes.

The emission rates estimated by IME method is given by Varon et al. (2018)

$$Q = \frac{U_{\mathrm{eff}} \cdot \mathrm{IME}}{L} = \frac{U_{\mathrm{eff}} \cdot \sum_{(x,y)\in\mathbf{I}} \Delta\Omega(x,y) A(x,y)}{\sqrt{\sum_{(x,y)\in\mathbf{I}} A(x,y)}}, \tag{7}$$

where $\mathbf{I}$ represents the set of pixels identified as plume, $\Delta\Omega(x,y)$ represents the mass enhancement of pixel (x,y), $A(x,y)$ represents the area of pixel (x,y). The effective wind speed is a logarithmic functions with linear variations to 10 m wind speed U_{10}, where the parameters are fitted using the WRF-LES simulations (Varon et al., 2018). Since the IME/L value may vary with the plume pixel detection method, we fit the U_{eff} for two methods in Table 1, UNSEP and SEP, respectively. We generate a large set of plumes with different emission rates, wind speeds and mixing heights to fit the U_{eff} in linear relation to $\log U_{10}$. The result is $U_{\mathrm{eff}} = 0.55 \log U_{10} + 0.62$ m s^{-1} for UNSEP, and $U_{\mathrm{eff}} = 0.64 \log U_{10} + 0.94$ m s^{-1} for SEP.

The IME method requires the specification of plume pixels $\mathbf{I}$ within the observation. Similar to Varon et al. (2018), we utilize a combination of Student's t-test and 2D filters to detect plume pixels in the observation. However, this single-source approach tends to introduce excessive estimation when there is more than one source, thereby hindering comparative analyses between the direct application of IME without separation (denoted as UNSEP) and the proposed separation and quantification approach

(denoted as SEP). To mitigate this issue, we propose a straightforward pixel detection process to make the results of UNSEP comparable to SEP. This process, named as connectivity filtering, is based on pixel connectivity analysis, a morphological image processing technique. For a source of interest, the pixels in its nearest connected structures are attributed to the source, designated as $\mathbf{I}$, while the remaining detected plume pixels are disregarded.

2.2 Synthesized observation

2.2.1 Methane plume simulation

We performe large eddy simulation using WRF-LES to synthesize observations for the evaluation. The LES is a promising methodology for solving the Navier-Stokes equation and is widely employed to simulate the dispersion in the ABL (Stoll et al., 2020). The WRF-LES can perform simulations that show good agreement with observations (Brunner et al., 2023) and is thus widely applied in the field of spaceborne GHG monitoring (Varon et al., 2018; Cusworth et al., 2019; Brunner et al., 2023).

WRF-LES is utilized to simulate 3D volume concentration of methane (in kg m^{-3}) from a point source, where the methane is modeled as passive tracer (Nottrott et al., 2014). We add a trace gas dispersion function with open boundary conditions by modifying the source code of the WRF 4.4 ideal LES experiment. Similar to Varon et al. (2018), methane plumes are simulated with a mean geostrophic wind of 1, 3, 5, 7 or 9 m s^{-1}; an inversion height of 500, 800 or 1100 m; a simulation region of 3.5 km x 6 km (across and along wind) with horizontal and vertical resolutions of 20 m and 10 m, respectively. The initial temperature is set as 293 K in the mixed layer, with a lapse rate of 0.12 K m^{-1} above the inversion height. The surface sensible heat flux is set as 100 W m^{-2}, respectively. The model is run for 3 hours for spin up and 2 hours for registration with 30 s intervals. The trace gas emission rate is set as 1kg s^{-1}. The simulated concentration is scalable with source emission rates, as simulated by passive trace gas dispersion.

The simulated 3D volume concentration snapshots are then integrated by each column weighted by column averaging kernel (Bovensmann et al., 2010; Jongaramrungruang et al., 2019). The column averaging kernel is a vector representing the vertical sensitivity distribution of the instrument and retrieval algorithm, and it is here considered to be vertically uniform. The resulting 2D column mass enhancements are then subjected to additive Gaussian noise, considering instrumental and retrieval uncertainty. The noise is given as a percentage of methane's mean dry column concentration, which is considered 1.8 ppm (i.e., ≈ 10.3 g m^{-2} at 1 atm, dry air). The influence of the methane background is not considered and the synthesized enhancements are only attributed to plume and noise in this work.

2.2.2 Synthetic observations

To evaluate the possible impact of plume overlapping on quantification and the performance of the proposed separation method, we performed observation system simulation experiments (OSSEs) with simulated mass columns by WRF-LES. The OSSEs are widely applied to evaluate the spaceborne GHG source detection and quantification abilities by simulating observed spectral radiations or retrieved concentrations (Bovensmann et al., 2010; Kuhlmann et al., 2019; Varon et al., 2018). OSSEs with realistic LES simulations, accounting for actual surface topography and meteorological conditions (Stoll et al., 2020), are

preferable for specific source targets, however, the computational cost can be expensive, considering massive point source targets with highly heterogeneous spatial and emission conditions, e.g., targets in Duren et al. (2019). One feasible approach is to sum multiple simulated column mass images after rotations, shiftings and concentration scalings while assuming the turbulence variations among multiple images are negligible. This approach allows for simulating sources with arbitrary emission rates, spatial and meteorological conditions, allowing much lower computation cost and thus reducing linear time complexity ($O(N)$) to nearly constant ($O(1)$) for simulating N sources when N is large enough.

To synthesize an image of concentration enhancement observation with multiple sources, we first establish an easting/northing Cartesian system where the x-axis points east and the y-axis points north. The field of view (FoV) is square with sides at the length of 6 km and parallel to the axes, centred at $(0, 0)$ of the Cartesian system. Then, the 2D column mass snapshots are randomly selected with the given wind speed and mixing depth. These snapshots are then scaled according to the emission rate of each source. Then, to rotate and shift the snapshots for an observation, we traverse all the pixels in the observation and accumulate their mapping pixels in each snapshot. For a given pixel of the observation at (x, y), the mapping pixel indexing in the nth snapshot is given by

$$\begin{bmatrix} i'_n \\ j'_n \end{bmatrix} = \begin{bmatrix} \cos\theta & \sin\theta \\ -\sin\theta & \cos\theta \end{bmatrix} \begin{bmatrix} x - x_n \\ y - y_n \end{bmatrix} \cdot \begin{bmatrix} \frac{1}{\Delta x} \\ \frac{1}{\Delta y} \end{bmatrix} + \begin{bmatrix} I_{\text{source}} \\ J_{\text{source}} \end{bmatrix}, \tag{8}$$

where θ represents the wind angle to a-axis; (x_n, y_n) represents the location of source n; Δx and Δy represent the horizontal resolutions in WRF-LES; $(I_{\text{source}}, J_{\text{source}})$ represent the location of the source pixel in WRF-LES. The indices (i'_n, j'_n) are then rounded, thus completing the nearest neighbour interpolation. Here, considering the small size of the plume and the domain, we adopt a unified wind velocity across the domain.

2.2.3 Observation scenarios

We test our separation method under three different scenarios, namely Exp1-3, each consisting of trials with various experiment settings. Examples of each scenario are shown in Fig. 2. Exp1, the single-source scenario, comprises a full factorial experiment of environmental factors, source factors and observation factors to evaluate the performance of quantifying methods. Exp2, the dual-source scenario, comprises a full factorial experiment with several overlapping-related factors to analyze the impact of plume overlapping, as well as to evaluate the performance of separation and quantification methods. Exp3, the random source scenario, comprises a Monte Carlo test to further evaluate the separation and quantification methods.

In Exp1, a single source is placed in the centre of the simulation domain and a full factorial experiment is conducted to test the performance of the quantifying method under all combinations of multiple-factor levels. These factors include environmental factors (mixing depth at 500, 800, and 1100 m; wind speed at 1, 3, 5, 7, 9 m s^{-1}; wind direction at 0, 45°), source factor (emission rates ranging from 100 to 2000 kg h^{-1}), and observation factors (ground pixel size ranging from 25 to 200 m; retrieval uncertainty at 1, 3, and 5%). It is noteworthy that for observation factors, ground pixel size is determined by typical point source monitoring satellites, while retrieval uncertainty is established by satellites with ultra-fine spectral resolution, such as GHGSat (Varon et al., 2018).The wind direction is defined in the Cartesian coordinate system, and the retrieval uncertainty

is considered a 0-biased additive noise with standard deviation as a percentage of methane's mean dry column mass. Each combination is repeated for 10 times. The quantification performance of Gaussian plume fitting, unseparated IME (UNSEP) and separated IME (SEP) methods are evaluated. The results are elaborated in Section 3.1. Examples of the plume image under various conditions are shown in the supplement.

In Exp2, a secondary source is introduced as an interference source to produce overlapping, as to evaluate the impact on quantification and separation. Exp2 is also a full factorial experiment, where we fix the mixing depth at 800 m, the emission rates at 200 kg h^{-1}, the ground pixel size at 25 m, and the retrieval uncertainty at 1%. The rest factors include wind speed at 1, 3, 5, 7, 9 m s^{-1}; wind direction ranging from -90 to 90°; distance between ranging from 100 to 900 m; and the emission rates ratio between the secondary and the original source (Q_2/Q_1) ranging from 0 to 5. Each combination of trials is repeated 10 times. The quantification performance of single-source Gaussian plume fitting, multi-source Gaussian plume fitting, unseparated IME and separated IME methods are evaluated. The results are elaborated in Section 3.2. The comparable results with different ground pixel size and noise settings are shown in the supplement.

In Exp3, a Monte Carlo experiment is conducted to further assess the performance of the unseparated IME and separated IME methods. For each trial, one source is randomly sampled from the AVRIS-NG observed methane source list (Duren et al., 2019) and its geolocation and emission rate is thus specified. Likewise, additional neighbouring sources within the 6 km × 6 km domain are then included in the simulation. For simplicity, sources with emission rates lower than 25 kg h^{-1} (accounting for about 5% of the summation) are excluded from the list as they are considered too small to be accurately measured by spaceborne measurements, and their interference as background is also negelected. Additionally, we assume all the sources in the list exhibit persistence. This assumption is supported by the average confidence for persistence in the original list is 0.83. Additionally, it compensates for the manual removal of overlapping sources during the quality control phase conducted by the list maker. The winds to load the plumes are then obtained from the 10 m wind of the fifth generation of atmospheric reanalysis of the European Centre for Medium-Range Weather Forecasts (ECMWF-ERA5; Hersbach et al., 2020). We then match geostrophic wind using the 10 m wind (shown in the supplement). A random plume with the matched geostrophic wind is then added to the domain. The sampling time range for loading wind velocity covers the entire local noon in 2022. The wind velocity is considered uniform across the domain and is interpolated to the observation centre using 5-point inverse distance weighting such as Xu et al. (2022). To ensure that all generated source inside the domain is quantifiable, each side of the simulation frame is extended outward 2 km for a 10 km × 10 km domain. The plumes originated from outside the domain are considered well mixed and their interferences to the synthesized enhancements are not considered. This random experiment is repeated 2000 times. The quantification performances of the unseparated IME and separated IME methods are then evaluated and elaborated in Section 3.3.

2.3 EMIT observation

We also test our separation method on methane plumes retrieved by the Earth Surface Mineral Dust Source Investigation (EMIT) instrument installed on the International Space Station (ISS). The EMIT is a hyperspectral instrument capable of imaging spectroscopy in the visible to short wavelength infrared, with a nadir ground sampling distance of 30-80 m.(Green

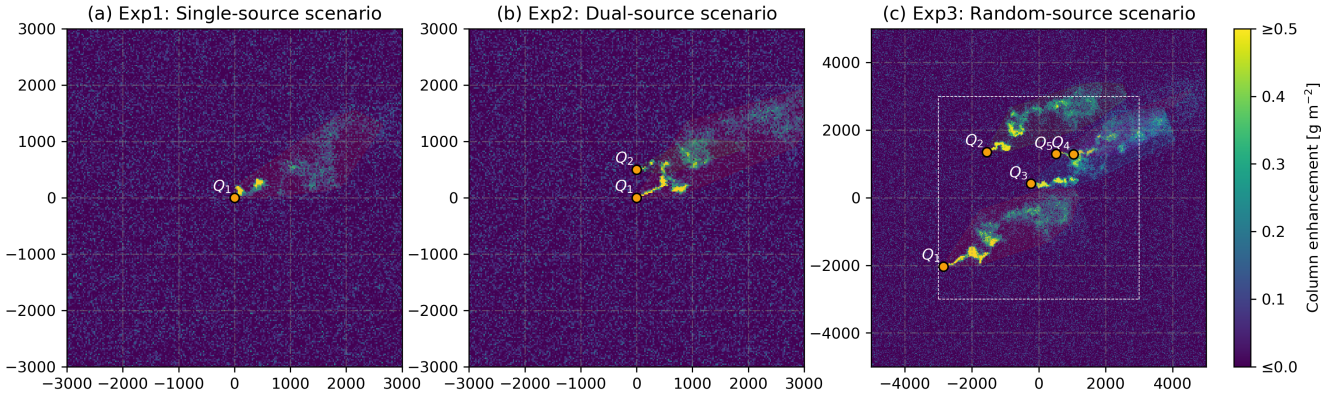

Figure 2. Examples for each experiment scenario of synthesized observations. The plots represent the synthesized methane column enhancements. Each semi-transparent polygon patch covers a plume, where the concentration is larger than the uncertainty. The dashed box in (c) encloses the area where random sources are generated. The emission rates vary between 200 kg h^{-1} and 2000 kg h^{-1}. In these examples, the ground pixel size is fixed at 25 m, while the retrieval uncertainty is set at 1%.

et al., 2020). The methane column enhancement data (EMITL2BCH4ENHv001) is expressed in units of parts per million meters (ppm m) and is retrieved using an adaptive matched filter technique. (Green et al., 2023b). Green et al. (2023a) also provides the corresponding identified plume complexes (EMITL2BCH4PLM v001), where the plumes sometimes overlap and thus form these clusters.

For the quantification, we first convert the concentration map from ppm m to kg m^{-2} (Sánchez-García et al., 2022). Then, we applied the separation method to extract plumes from each source, and the extracted plumes are then quantified by the IME method, as described in Section 2.1. The wind velocity for separation and quantification is interpolated from ERA5 as described in Section 2.2.3. The source locations are identified through visual inspection, and cross-verified with local ground facilities using high-resolution satellite map from Google Earth. Monte Carlo propagation is introduced to evaluate the uncertainty of the quantification and the systematic uncertainty of the IME method is not considered (Sánchez-García et al., 2022). For the Monte Carlo propagation, the input uncertainties include observation uncertainty from the corresponding EMITL2BCH4PLM data, and wind speed uncertainty estimated as the standard deviation of the nearest 5 points from ERA5.

2.4 Evaluation indicators

2.4.1 Overlapping indicator

To assess the degree of plume overlapping, a mass overlapping index is proposed, defined as the ratio of the mass integration of the interference sources to that of the primary source. The mass overlapping index for source i of N sources is given by

$$\mathrm{OI}_{\mathrm{mass}_i} = \frac{\sum_{(x,y)\in\mathbf{I}}[(\sum_{n=1}^{N}\Delta\Omega_n(x,y) - \Delta\Omega_i(x,y))\cdot A(x,y)]}{\sum_{(x,y)\in\mathbf{I}}\Delta\Omega_i(x,y)A(x,y)} \tag{9}$$

where $\mathbf{I}$ denotes the plume pixel of source i. Higher $\mathrm{OI}_{\mathrm{mass}_i}$ denotes that the plume of source i is subject to more severe interference.

2.4.2 Emission rates estimation indicators

The quantification of methane source is considered as solving a parameter estimation problem. We introduce the R^2, coefficient of determination, to indicate the overall prediction accuracy. Furthermore, as R^2 has a relatively poor ability to explain samples with small true values, absolute percentage error (APE) is introduced to indicate the estimation error of a single sample, and mean absolute percentage error (MAPE) is introduced to indicate the overall estimation error. The definitions of R^2, APE and MAPE are given by

$$R^2 = 1 - \frac{\sum_{n=1}^{N}(\hat{Q}_n - Q_n)^2}{\sum_{n=1}^{N}(\bar{Q} - Q_n)^2}, \tag{10}$$

$$\mathrm{APE}_n = \Big|\frac{\hat{Q}_n - Q_n}{Q_n}\Big|, \tag{11}$$

$$\mathrm{MAPE} = \frac{1}{N}\sum_{n=1}^{N}\Big|\frac{\hat{Q}_n - Q_n}{Q_n}\Big|, \tag{12}$$

respectively, where Q_n and $\hat{Q}_n$ represent the true emission rate and predicted emission rate, respectively, of source n; $\bar{Q}$ is the average of true emission rates; N represents the number of sources in the experiments.

3 Results

3.1 Quantification results on single source

In Exp1, we evaluate the baseline performance of various quantification methods, including the emission rates derived directly from the Gaussian plume fitting, unseparated and direct IME quantification (denoted as UNSEP), and quantification after applying the separation method (denoted as SEP), using a full factorial experiment. The overall quantification errors (MAPE) for the three quantification methods are 0.89, 0.30, and 0.40, respectively. The distributions of quantification errors, in terms of absolute percentage error (APE), with respect to different simulation factors in Exp1, are shown in Fig. 3.

As shown in Fig. 3(a), the APE of all three methods exhit nearly linear incresing trends with respect to pixel size, with Pearson's correlation coefficients (R) of 0.24, 0.18 and 0.21, and all p-values are less than 0.01. Similar trends are also shown

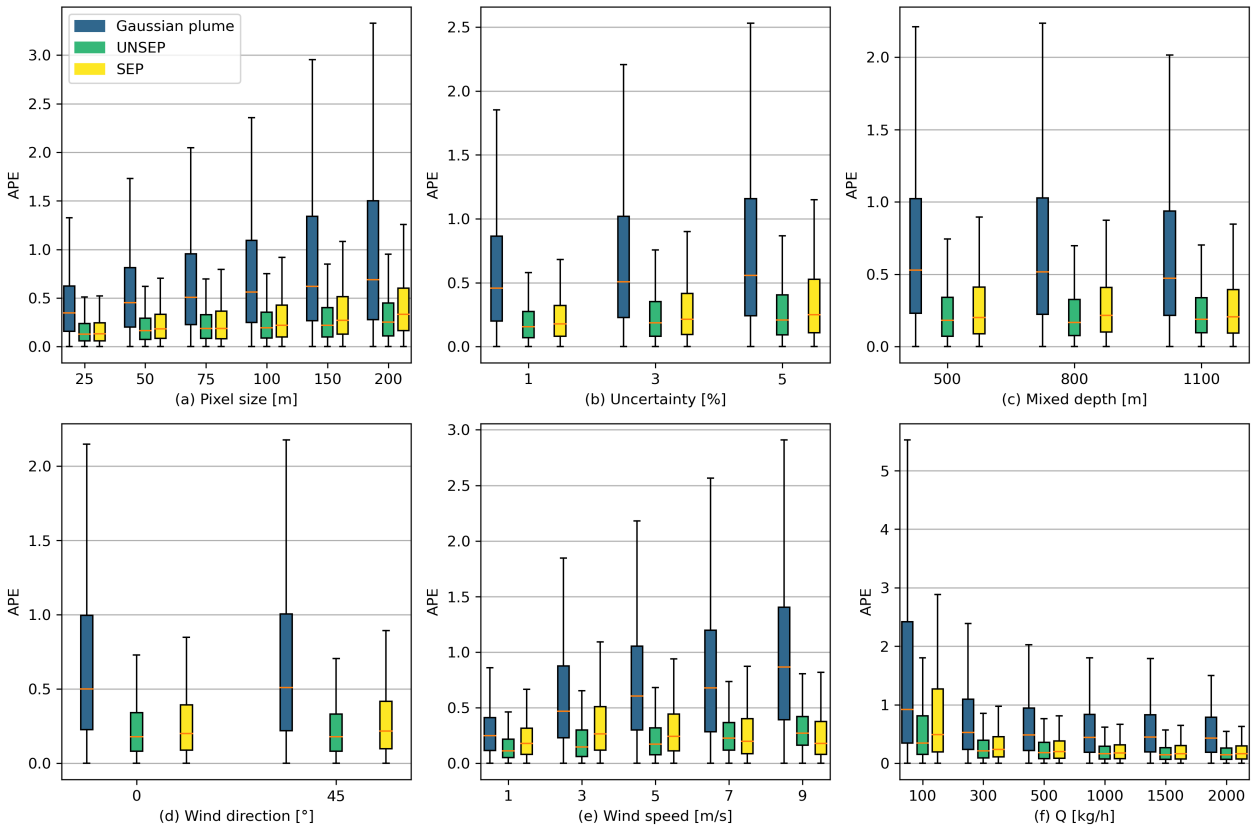

Figure 3. Distribution of quantification APE under various experimental parameters in Exp1. The orange dashes denote the medians of APE; the boxes denote the range between the lower and upper quartiles (Q1 and Q3); $\perp$ and $\top$ extend from the box by 1.5 times the inter-quartile range (IQR). The quantification errors in APE of Gaussian plume fitting, unseparated IME (UNSEP) and separated IME (SEP) methods are represented with legend.

in Fig. 3(b), where the APE of three methods increase slightly with respect to uncertainty ($R = 0.16, 0.13, 0.14$; $p < 0.01$). As shown in Fig. 3(c) and Fig. 3(d), the variance of APE with respect to mixed depth and wind direction is minor. As shown in 3(e), the APE of Gaussian plume and UNSEP increase with respect to the wind speed. However, the APE of the SEP reaches the maximum at the wind speed of 3 m s^{-1}. With increasing wind speed, SEP exhibits lower quantification error than UNSEP in 9 m/s. As shown in Fig. 3(f), the quantification error of all three method decrease with the emission rates, and shows a sub-linear trend.

3.2 Quantification results on dual sources

In Exp2, we introduce an interference source as to create overlapping for the full factorial experiment. After introducing an interference source, the MAPE of single-source Gaussian plume fitting increases from 0.45 to 1.23, while the increases of

multi-source Gaussian plume model are negligible, which remains 0.45. Similarly, the UNSEP increases from 0.15 to 0.83, while the SEP only increases from 0.30 to 0.38.

As demonstrated in Fig. 4, the SEP shows the best quantification performance in most cases, followed by multi-source Gaussian plume fitting, UNSEP and single-source Gaussian plume fitting, in terms of MAPE. With decreasing wind speed, the errors of quantification results by multi-source Gaussian plume fitting become comparable to that of SEP. When the wind speed is 1 m s^{-1}, the quantification results of multi-source Gaussian plume fitting is slight better than SEP. As distance increases or interference strength (Q_2/Q_1) decreases, plumes are less likely to overlap, leading to UNSEP outperforming SEP. At 900 m distance or interference strength decreasing to 0.5, UNSEP achieves the best quantification performance.

The multiple source Gaussian plume and SEP exhibit better quantification performance on overlapping plumes as interference strength intensifies. Besides, both multi-source Gaussian plume fitting and SEP show minor variations over factors including wind direction, wind speed, distance between two sources and interference strength. In contrast, single-source Gaussian plume fitting and UNSEP are more susceptible to these factors, with their performances deteriorating as wind direction increasingly aligns with the line connecting the sources, wind speed decreases (for UNSEP), wind speed increases (for single-source Gaussian plume fitting), distance decreases, and interference intensifies. Similar trends are observed with varying observation pixel sizes and retrieval noise, as demonstrated in our further experiments (shown in the supplement).

3.3 Quantification results on random sources

In Exp3, we focus on comparing the UNSEP and SEP in a more realistic Monte Carlo simulation. Factors including source locations, emission rates and wind velocities are randomly selected from real distributions. The sampled factors demonstrate good agreement in terms of source emission rates (Fig. 5(a)), and wind speed (Fig. 5(b)) with the real distributions of the entire source list. The sampled emission rates follow a log-normal distribution, with mean of 172.2 kg h^{-1} and standard deviation of 340.8 kg h^{-1}. As shown in Fig. 5(c), 53.7% of the frames cover one source, 24.6% of the frames cover two sources, and 21.7% of the frames cover more than two sources. On average, there are 2.33 sources per frame (6 km $\times$ 6 km).

Fig. 6 shows the quantification results of unseparated and separated IME quantifications. The results of SEP demonstrate improvements in R^2 from 0.71 to 0.83 compared to UNSEP, and a decrease in the quantification error (MAPE) from 1.46 to 0.44. We also find that SEP is notably more accurate in estimating of low-emission sources compared to UNSEP.

To further investigate the distribution of overlapping and the performance of UNSEP and SEP in handling overlapping, we demonstrate quantification error over the source overlapping index. The overlapping index $\mathrm{OI_{mass}}$ ranges from 0 to 6.09. Only 36.0% of sources are completely isolated from other sources and their overlapping index $\mathrm{OI_{mass}}$ is 0; half of the sources are with $\mathrm{OI_{mass}} > 0.02$; and 4.3% of sources are be subjected to overlapping with $\mathrm{OI_{mass}} \geq 1$. We observe a near linear relation relationship between APE of UNSEP and $\mathrm{OI_{mass}}$ (Pearson's $R = 0.45$, $p < 0.01$), and the regression result can be expressed as $\mathrm{APE_{UNSEP}} = 2.76 \cdot \mathrm{OI_{mass}} + 1.34$. We define severe overlapping as occurring when the APE exceeds twice the intercept. Then, this results in a $\mathrm{OI_{mass}}$ threshold of 0.41, indicating that 28.9% of the sources experience severe overlapping. In comparison, the corresponding $\mathrm{OI_{mass}}$ threshold of SEP is 3.00 ($\mathrm{APE_{SEP}} = 0.15 \cdot \mathrm{OI_{mass}} + 0.45$; Pearson's $R = 0.13$, $p < 0.01$), which

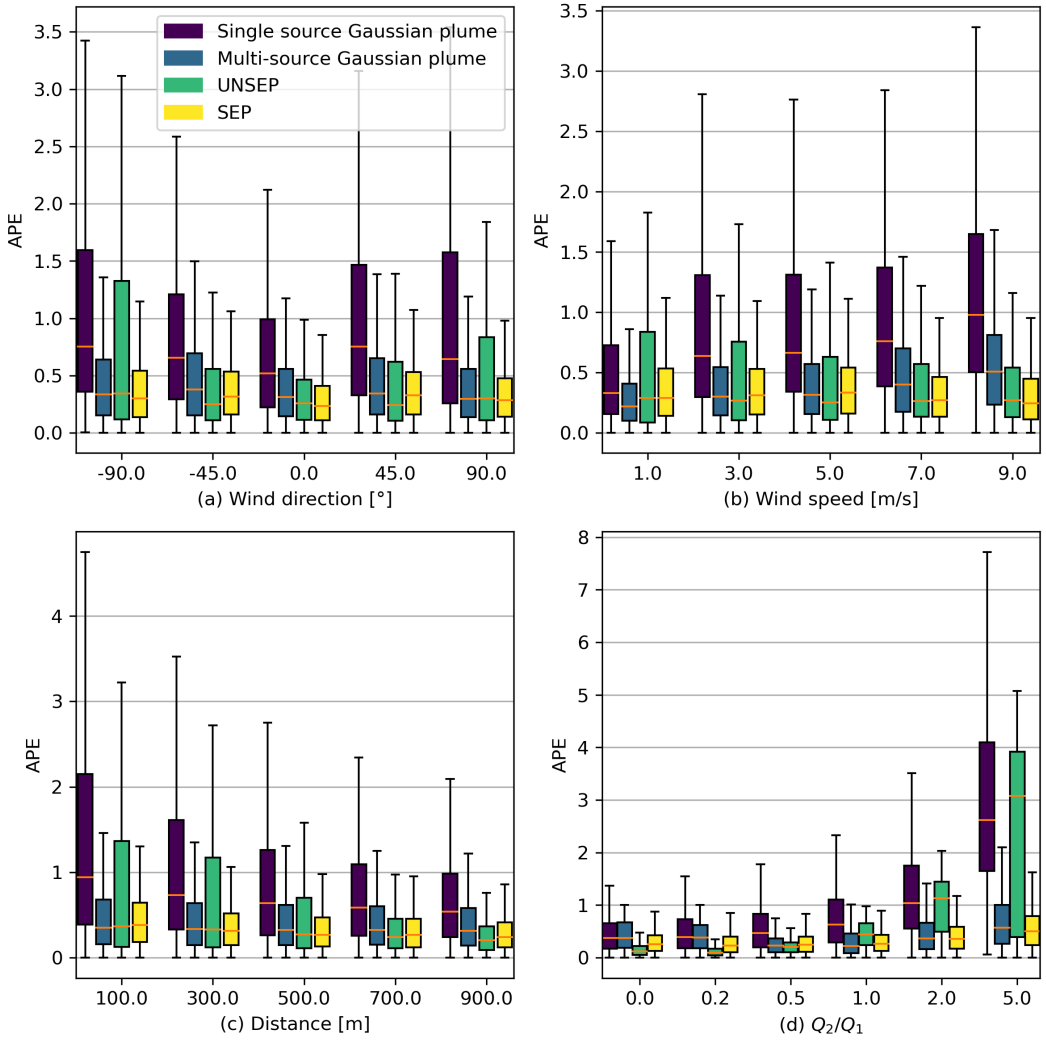

Figure 4. Distribution of quantification APE with respect to various experimental factors in Exp2.

only accounts 0.5% of all sources. This indicates the effect of overlapping is largely depressed by SEP and thus results in robust quantification.

3.4 Quantification on EMIT observation

In this section, we evaluate our separation and quantification method using real satellite observation of EMIT. We focus on a specified cluster of plumes observed by EMIT on 15th August 2022 at 4:28 (UTC) in Turkmenistan, near the Goturdepe oil and gas production field. The sources in this location are spatially aggregated and create significant plume overlapping (see Fig. 8). Through manual inspection and high-resolution satellite imagery verification, we identify 6 sources within the cluster.

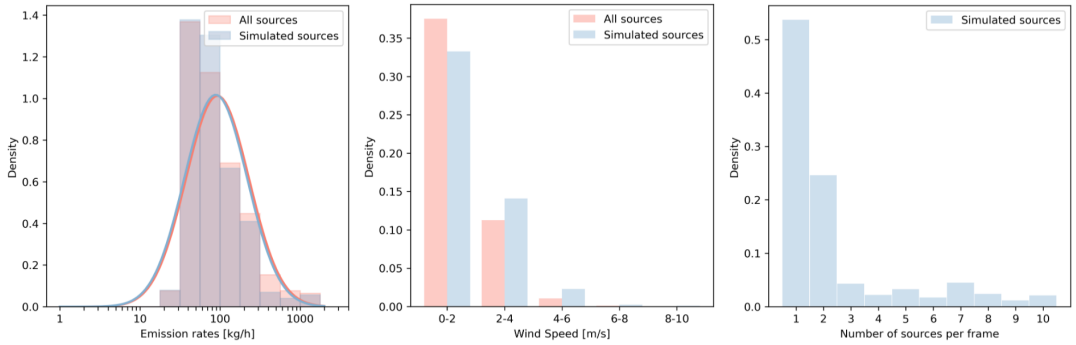

Figure 5. Statistical description of the factors in the Monte Carlo experiment (Exp3). denotes the distribution of all sources from AVIRIS-NG methane source inventory and the corresponding local noon wind speed distribution in the entire year of 2022. denotes the distribution of the selected sources in Exp3.

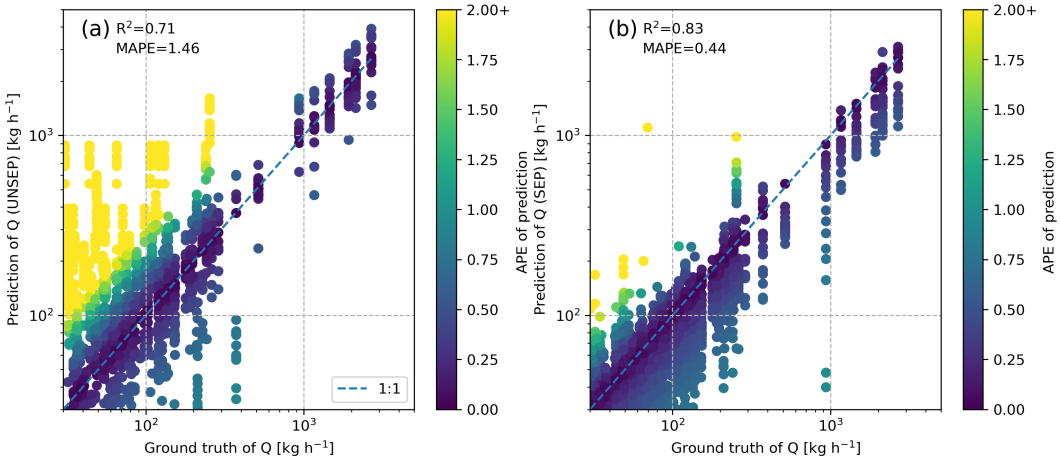

Figure 6. Comparison between quantification results of (a) unseparated quantification and (b) separated quantification in Exp3.

The emission rates of each source is quantified using our separated quantification method. Additionally, we quantify the entire cluster as a whole using the conventional IME method (UNSEP without connectivity filtering in Table 2.1.4).

The quantification results are shown in Table 2. The estimated emission rates for each source range from 1.64 to 5.20 t h^{-1}. We compare our estimated emission rates with previous research. We find that source Q_3 has also been quantified by Irakulis-Loitxate et al. (2022) and Sánchez-García et al. (2022) and their estimations for Q_3 are 1.4 ± 0.4 t h^{-1} and 5.0 ± 2.2 t h^{-1}, respectively. There is a gap of more than two years between these two estimations, and their estimations demonstrate significant difference. Our estimation for Q_3 on 15th August 2022 is 3.34 ± 0.90 t h^{-1}, which is comparable to the previous estimations. The summation of separated quantification results on the 6 sources is 16.77 ± 4.65 t h^{-1}. In comparison, the quantification

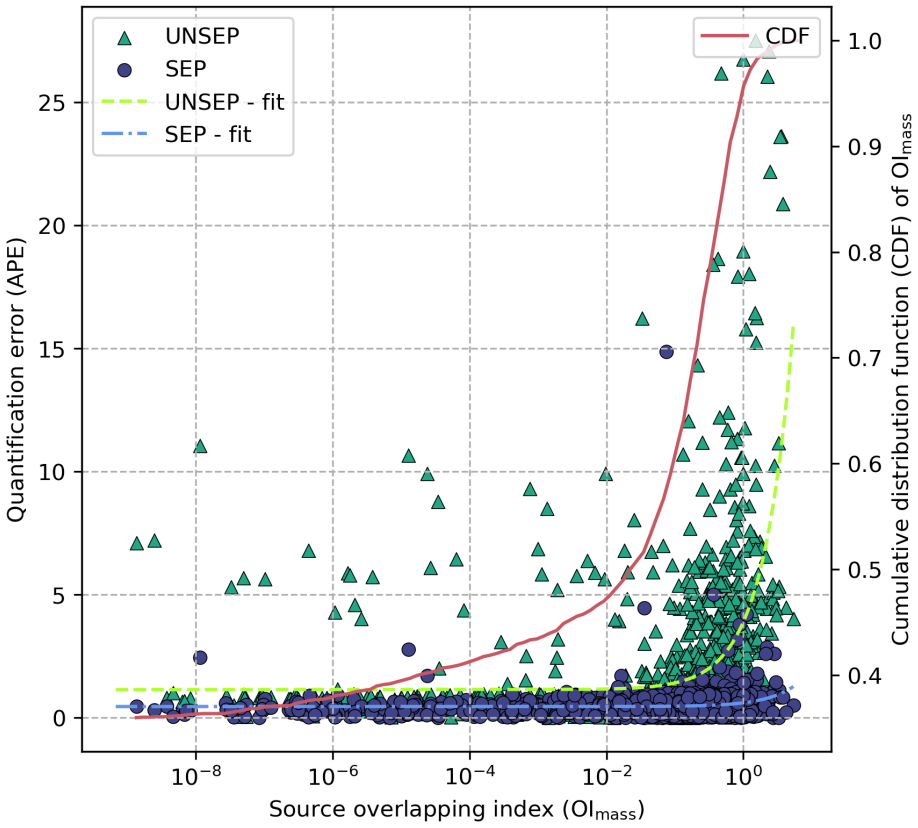

Figure 7. Comparison between quantification results and source overlapping index ($\mathrm{OI}_{\mathrm{mass}}$). The dash-line represents the linear fitted quantification error of UNSEP with respect to $\mathrm{OI}_{\mathrm{mass}}$. The red solid line represents the cumulative distribution function of $\mathrm{OI}_{\mathrm{mass}}$.

result of the whole cluster is 21.06 ± 5.51 t h^{-1}, which is higher than the summation but their difference are consistent within margins of error. It's reasonable as pixels in separated quantification may not be attributed to any source and thus excluded in the final quantification, leading to underestimations.

4 Discussion and conclusions

In this study, we compared the baseline quantification performance of the Gaussian plume model with two IME-based methods (UNSEP and SEP) for spaceborne methane point source monitoring in Exp1 (see Section 3.1). Our findings indicate that the IME methods outperform the Gaussian plume model in the small scales with ground pixel sizes up to 200 m. Additionally, we observed weak positive linear relationships of the quantification error of all three methods with respect to both ground pixel size and retrieval uncertainty.

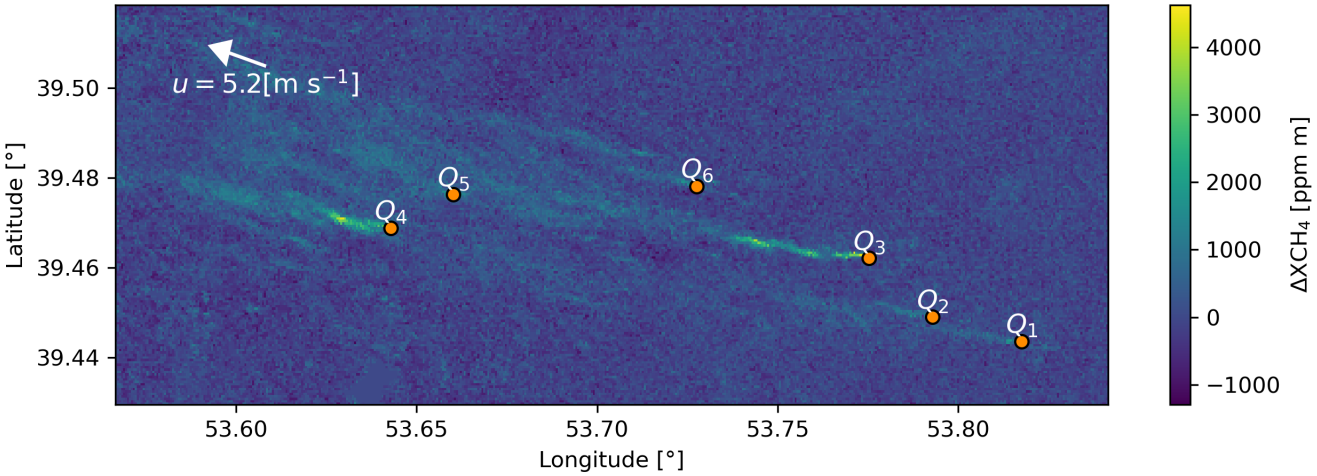

Figure 8. Overlapping plumes observed by EMIT on 15 August 2022 at 4:28 (UTC). This image is from the dataset EMITL2BCH4ENH v001, which is publicly available at https://lpdaac.usgs.gov/products/emitl2bch4enhv001/.

Table 2. Quantification results of EMIT observation. 6 sources are manually identified and quantified. The quantification results summation of separated IME method over each source separately (Summation) is compared to the results of unseparated IME method over the whole methane plume cluster (Whole).

Source ID	Source location	Estimated emission rates [t h^{-1}]	Reference emission rates [t h^{-1}]
Q_1	(39.4436°N, 53.8176°E)	1.64 ± 0.49	
Q_2	(39.4490°N, 53.7929°E)	1.35 ± 0.42	
Q_3	(39.4620°N, 53.7753°E)	3.34 ± 0.90	1.4 ± 0.4 *
			5.0 ± 2.2**
Q_4	(39.4687°N, 53.6428°E)	5.20 ± 1.38	
Q_5	(39.4762°N, 53.6602°E)	1.69 ± 0.50	
Q_6	(39.4781°N, 53.7276°E)	3.55 ± 0.95	
Summation		16.77 ± 4.65	
Whole		21.06 ± 5.51	

* Observed by PRISMA on 27 March 2020 (Irakulis-Loitxate et al., 2022).

** Observed by WorldView-3 on 10 April 2022 (Sánchez-García et al., 2022).

Then we investigated the impact of plume overlapping on the quantification. We found that plume overlapping increases quantification errors in Exp2. Specifically, the MAPE for the UNSEP method increased from 0.15 to 0.83, and for single-source Gaussian plume fitting, it increased from 0.45 to 1.23 when compared to cases with no interference (see Section 3.2).

Factors such as closer source intervals and disproportion emission rates will enlarge these defects. Overlapping plumes can produce connective pixels that cover multiple sources, which are ambiguous to be attributed. Simply eliminating these pixels will result in increasing missed detections and quantification errors. In addition, the relatively sparse spatial resolution of spaceborne methane monitoring techniques compared to airborne techniques can increase the proportion of these ambiguous pixels. The findings from the Monte Carlo experiment of Exp3 indicate that plume overlapping can affect up to 18% of the sources, resulting in a doubling of errors for unseparated-IME quantification (see Section 3.3). As a result, it's essential to find and attribute pixels in overlapping plumes correctly for spaceborne quantification.

To tackle this issue, we introduced a heuristic optimization algorithm to perform parameter estimations for the 2D multi-source Gaussian plume model. Based on the outputs of this model with the estimated parameters, we assigned the mass to sources according to the modeled concentrations by each pixel. In this way, we separated an overlapping-plume image into several single-plume images. This "soft segmentation" shows better performance in plume pixel detection on overlapping plumes than "hard segmentation" methods, e.g., the plume detection method by Varon et al. (2018), which assigns all the mass in a pixel to a single source while the mass may originate from multiple sources. Results in the Monte Carlo experiment (Exp3) show that the application of separation is effective in quantification, where MAPE decreases from 1.46 to 0.45, and R^2 increases from 0.71 to 0.84, compared to quantification without separation (see Section 3.3).

Additionally, our separation model can perform independent estimation for attributes such as wind speed and direction, and source locations, which make the separation robust to the uncertainty in auxiliary data. Although the emission rates as parameters of the 2D multi-source Gaussian plume model are estimated, they are only used for separation instead of quantification. As our experiment results in Exp1 and Exp2 shows, Gaussian plume fitting exhibit higher systematical uncertainty than the IME method on quantifying fine-scale methane plumes. It need to be noticed that, in our experiment, the quantification error of Gaussian plume increase with pixel size and is constantly higher than the IME methods as shown in Exp1. It is slightly different from Varon et al. (2018); Jongaramrungruang et al. (2019), which shows that plume shows better approximation of Gaussian form with increasing pixel size above 300 meters. One explaination for the inability to pinpoint the turning point of performance enhancement in Gaussian plume fitting is the limited size of our simulation domain. As we increase the pixel size, the number of pixel samples decreases, which counteracts the advantages of averaging eddies using larger pixels, thereby impeding the performance improvement of the Gaussian plume fitting. A comprehensive exploration of the trade-offs between Gaussian plume and IME methods may require large-scale, high-resolution LES simulations, and it is beyond the scope of this paper.

In the experiment on real satellite observations (see Section 3.4), firstly, we notice that identifying source locations correctly is crucial for separation and quantification. Although we verified the source with satellite imagery, it still appears less precise. Utilizing detailed facility-level inventories, such as VISTA-CA, could greatly help source detection, separation and quantification. Additionally, for previously unknown emission sources, integrating multimodal information, including pipeline maps and simultaneous facility flare observations can also be introduced for accurate identifying (Irakulis-Loitxate et al., 2022). Secondly, we also notice that there are unignorable differences in source quantification results across research, as shown in Section 3.4. The temporal variability in source emissions and the associated uncertainty in quantification are coupled, posing

challenges to cross-verification among observations. This suggests the need for further verification with ground truth data. Thirdly, we find that in some cases the plumes exhibit a large deviation from the WRF-LES simulation, especially in complex terrains, such as valleys. In this case, using uniform wind assumptions may also lead to the overestimation of the performance of the IME quantification method as well as the separation method.

In this study, we proposed a separation and quantification approach, which combines Gaussian plume and IME method, to quantify the overlapping plumes from multiple facility-level point sources in spaceborne methane observations. As implied by the VISTA-CA inventory and AVIRIS-NG observed methane source list, the methane point sources can be spatially aggregated in some places, meaning that the plume overlapping may be non-negligible. This demerit will constrain the quantification scope of spaceborne GHG monitoring techniques. As a result, our separation method can be important to spaceborne methane monitoring for constructing or verifying facility-level emission inventories (e.g., Duren et al., 2019), as well as environmental administration departments. For future research, a dispersion model, which is more representative of real transient plumes, can be introduced to improve the separation performance. The interferences of background methane are not considered in this work, and future work may consider using realistic backgrounds to account the irregular noise, such as Jongaramrungruang et al. (2022) and Gorroño et al. (2022). A series of tests on more realistic simulations, as well as real observations, should also be performed for further validation.

Code availability. The original version of the WRF source code is publicly available at https://www.mmm.ucar.edu/models/wrf; the source code of the proposed separation method in Section 2.1 is available upon request.

Data availability. The VISTA-CA inventory is publicly available at https://doi.org/10.3334/ORNLDAAC/1726; the AVIRIS-NG observed methane source list is publicly available as the supplementary information at https://doi.org/10.1038/s41586-019-1720-3; the ECMWF-ERA5 reanalysis meteorological data are publicly available at https://www.ecmwf.int/en/forecasts/dataset/ecmwf-reanalysis-v5; the EMIT methane enhancement data are publicly available at https://lpdaac.usgs.gov/products/emitl2bch4enhv001/; the EMIT estimated methane plume complexes are publicly available at https://lpdaac.usgs.gov/products/emitl2bch4plmv001/; the LES-simulated 2D plume snapshots are available upon request.

Author contributions. YP designed and implemented the study, as well as composed the draft. GL, LT and SG conceptualized the objective of this study. DH and GL reviewed and edited the manuscript. All authors reviewed the manuscript.

Competing interests. The author has declared that there are no competing interests.

Acknowledgements. We are grateful to the affiliated group(s) at JPL for generously sharing their findings from AVIRIS-NG and EMIT. We also express our appreciation to NCAR for their efforts in the development and provision of the WRF code. Furthermore, we extend special gratitude to the two anonymous reviewers, particularly one who provided numerous practical insights and advice.

Financial support. This research has been supported by the National Key Research and Development Program of China (grant no.2022YFB3904800) and the Youth Innovation Promotion Association of CAS (grant no.29Y0ZKQCYG01).

References

Allen, C. T., Haupt, S. E., and Young, G. S.: Source Characterization with a Genetic Algorithm–Coupled Dispersion–Backward Model Incorporating SCIPUFF, Journal of Applied Meteorology and Climatology, 46, 273–287, https://doi.org/10.1175/JAM2459.1, 2007.

Bovensmann, H., Buchwitz, M., Burrows, J. P., Reuter, M., Krings, T., Gerilowski, K., Schneising, O., Heymann, J., Tretner, A., and Erzinger, J.: A Remote Sensing Technique for Global Monitoring of Power Plant CO_2 Emissions from Space and Related Applications, Atmospheric Measurement Techniques, 3, 781–811, https://doi.org/10.5194/amt-3-781-2010, 2010.

Briggs, G. A.: Diffusion Estimation for Small Emissions. Preliminary Report, Tech. Rep. TID-28289, National Oceanic and Atmospheric Administration, Oak Ridge, Tenn. (USA). Atmospheric Turbulence and Diffusion Lab., https://doi.org/10.2172/5118833, 1973.

Brunner, D., Kuhlmann, G., Henne, S., Koene, E., Kern, B., Wolff, S., Voigt, C., Jöckel, P., Kiemle, C., Roiger, A., Fiehn, A., Krautwurst, S., Gerilowski, K., Bovensmann, H., Borchardt, J., Galkowski, M., Gerbig, C., Marshall, J., Klonecki, A., Prunet, P., Hanfland, R., Pattantyús-Ábrahám, M., Wyszogrodzki, A., and Fix, A.: Evaluation of Simulated CO_2 Power Plant Plumes from Six High-Resolution Atmospheric Transport Models, Atmospheric Chemistry and Physics, 23, 2699–2728, https://doi.org/10.5194/acp-23-2699-2023, 2023.

Calvo Buendia, E., Tanabe, K., Kranjc, A., Baasansuren, J., Fukuda, M., Ngarize, S., Osako, A., Pyrozhenko, Y., Shermanau, P., and Federici, S.: 2019 Refinement to the 2006 IPCC Guidelines for National Greenhouse Gas Inventories, vol. 1, Intergovernmental Panel on Climate Change, 2019.

Cervone, G., Franzese, P., and Grajdeanu, A.: Characterization of Atmospheric Contaminant Sources Using Adaptive Evolutionary Algorithms, Atmospheric Environment, 44, 3787–3796, https://doi.org/10.1016/j.atmosenv.2010.06.046, 2010.

Cusworth, D. H., Jacob, D. J., Varon, D. J., Miller, C. C., Liu, X., Chance, K., Thorpe, A. K., Duren, R. M., Miller, C. E., Thompson, D. R., Frankenberg, C., Guanter, L., and Randles, C. A.: Potential of Next-Generation Imaging Spectrometers to Detect and Quantify Methane Point Sources from Space, Atmospheric Measurement Techniques, 12, 5655–5668, https://doi.org/10.5194/amt-12-5655-2019, 2019.

Cusworth, D. H., Duren, R. M., Thorpe, A. K., Tseng, E., Thompson, D., Guha, A., Newman, S., Foster, K. T., and Miller, C. E.: Using Remote Sensing to Detect, Validate, and Quantify Methane Emissions from California Solid Waste Operations, Environmental Research Letters, 15, 054 012, https://doi.org/10.1088/1748-9326/ab7b99, 2020.

Duren, R. M., Thorpe, A. K., Foster, K. T., Rafiq, T., Hopkins, F. M., Yadav, V., Bue, B. D., Thompson, D. R., Conley, S., Colombi, N. K., Frankenberg, C., McCubbin, I. B., Eastwood, M. L., Falk, M., Herner, J. D., Croes, B. E., Green, R. O., and Miller, C. E.: California's Methane Super-Emitters, Nature, 575, 180–184, https://doi.org/10.1038/s41586-019-1720-3, 2019.

Ermak, D. L.: An Analytical Model for Air Pollutant Transport and Deposition from a Point Source, Atmospheric Environment (1967), 11, 231–237, 1977.

Frankenberg, C., Platt, U., and Wagner, T.: Iterative Maximum a Posteriori (IMAP)-DOAS for Retrieval of Strongly Absorbing Trace Gases: Model Studies for CH4 and CO2 Retrieval from near Infrared Spectra of SCIAMACHY Onboard ENVISAT, Atmospheric Chemistry and Physics, 5, 9–22, https://doi.org/10.5194/acp-5-9-2005, 2005.

Frankenberg, C., Thorpe, A. K., Thompson, D. R., Hulley, G., Kort, E. A., Vance, N., Borchardt, J., Krings, T., Gerilowski, K., Sweeney, C., Conley, S., Bue, B. D., Aubrey, A. D., Hook, S., and Green, R. O.: Airborne Methane Remote Measurements Reveal Heavy-Tail Flux Distribution in Four Corners Region, Proceedings of the National Academy of Sciences of the United States of America, 113, 9734–9739, https://doi.org/10.1073/pnas.1605617113, 2016.

Gorroño, J., Varon, D. J., Irakulis-Loitxate, I., and Guanter, L.: Understanding the Potential of Sentinel-2 for Monitoring Methane Point Emissions, Atmospheric Measurement Techniques Discussions, pp. 1–25, https://doi.org/10.5194/amt-2022-261, 2022.

Green, R., Thorpe, A., Brodrick, P., Chadwick, D., Elder, C., Villanueva-Weeks, C., Fahlen, J., Coleman, R. W., Jensen, D., Olsen-Duvall, W., Lundeen, S., Lopez, A., and Thompson, D.: EMIT L2B Estimated Methane Plume Complexes 60 m V001, https://doi.org/10.5067/EMIT/EMITL2BCH4PLM.001, 2023a.

Green, R., Thorpe, A., Brodrick, P., Chadwick, D., Elder, C., Villanueva-Weeks, C., Fahlen, J., Coleman, R. W., Jensen, D., Olsen-Duvall, W., Lundeen, S., Lopez, A., and Thompson, D.: EMIT L2B Methane Enhancement Data 60 m V001, https://doi.org/10.5067/EMIT/EMITL2BCH4ENH.001, 2023b.

Green, R. O., Mahowald, N., Ung, C., Thompson, D. R., Bator, L., Bennet, M., Bernas, M., Blackway, N., Bradley, C., Cha, J., Clark, P., Clark, R., Cloud, D., Diaz, E., Ben Dor, E., Duren, R., Eastwood, M., Ehlmann, B. L., Fuentes, L., Ginoux, P., Gross, J., He, Y., Kalashnikova, O., Kert, W., Keymeulen, D., Klimesh, M., Ku, D., Kwong-Fu, H., Liggett, E., Li, L., Lundeen, S., Makowski, M. D., Mazer, A., Miller, R., Mouroulis, P., Oaida, B., Okin, G. S., Ortega, A., Oyake, A., Nguyen, H., Pace, T., Painter, T. H., Pempejian, J., Garcia-Pando, C. P., Pham, T., Phillips, B., Pollock, R., Purcell, R., Realmuto, V., Schoolcraft, J., Sen, A., Shin, S., Shaw, L., Soriano, M., Swayze, G., Thingvold, E., Vaid, A., and Zan, J.: The Earth Surface Mineral Dust Source Investigation: An Earth Science Imaging Spectroscopy Mission, in: 2020 IEEE Aerospace Conference, pp. 1–15, https://doi.org/10.1109/AERO47225.2020.9172731, 2020.

Guanter, L., Irakulis-Loitxate, I., Gorrono, J., Sanchez-Garcia, E., Cusworth, D. H., Varon, D. J., Cogliati, S., and Colombo, R.: Mapping Methane Point Emissions with the PRISMA Spaceborne Imaging Spectrometer, Remote Sensing of Environment, 265, 112 671, https://doi.org/10.1016/j.rse.2021.112671, 2021.

Haupt, S., Young, G., and Allen, C.: A Genetic Algorithm Method to Assimilate Sensor Data for a Toxic Contaminant Release, Journal of Computers, 2, https://doi.org/10.4304/jcp.2.6.85-93, 2007.

Hersbach, H., Bell, B., Berrisford, P., Hirahara, S., Horányi, A., Muñoz-Sabater, J., Nicolas, J., Peubey, C., Radu, R., Schepers, D., Simmons, A., Soci, C., Abdalla, S., Abellan, X., Balsamo, G., Bechtold, P., Biavati, G., Bidlot, J., Bonavita, M., De Chiara, G., Dahlgren, P., Dee, D., Diamantakis, M., Dragani, R., Flemming, J., Forbes, R., Fuentes, M., Geer, A., Haimberger, L., Healy, S., Hogan, R. J., Hólm, E., Janisková, M., Keeley, S., Laloyaux, P., Lopez, P., Lupu, C., Radnoti, G., de Rosnay, P., Rozum, I., Vamborg, F., Villaume, S., and Thépaut, J.-N.: The ERA5 Global Reanalysis, Quarterly Journal of the Royal Meteorological Society, 146, 1999–2049, https://doi.org/10.1002/qj.3803, 2020.

Hopkins, F., Rafiq, T., and Duren, R.: Sources of Methane Emissions (Vista-CA), State of California, USA, https://doi.org/10.3334/ORNLDAAC/1726, 2019.

Hosseini, B. and Stockie, J. M.: Estimating Airborne Particulate Emissions Using a Finite-Volume Forward Solver Coupled with a Bayesian Inversion Approach, Computers & Fluids, 154, 27–43, https://doi.org/10.1016/j.compfluid.2017.05.025, 2017.

Hutchinson, M., Oh, H., and Chen, W.-H.: A Review of Source Term Estimation Methods for Atmospheric Dispersion Events Using Static or Mobile Sensors, Information Fusion, 36, 130–148, https://doi.org/10.1016/j.inffus.2016.11.010, 2017.

IPCC: Climate Change 2021: The Physical Science Basis. Contribution of Working Group I to the Sixth Assessment Report of the Intergovernmental Panel on Climate Change, vol. In Press, Cambridge University Press, Cambridge, United Kingdom and New York, NY, USA, https://doi.org/10.1017/9781009157896, 2021.

Irakulis-Loitxate, I., Guanter, L., Maasakkers, J. D., Zavala-Araiza, D., and Aben, I.: Satellites Detect Abatable Super-Emissions in One of the World's Largest Methane Hotspot Regions, Environmental Science & Technology, 56, 2143–2152, https://doi.org/10.1021/acs.est.1c04873, 2022.

Jacob, D. J., Varon, D. J., Cusworth, D. H., Dennison, P. E., Frankenberg, C., Gautam, R., Guanter, L., Kelley, J., McKeever, J., Ott, L. E., Poulter, B., Qu, Z., Thorpe, A. K., Worden, J. R., and Duren, R. M.: Quantifying Methane Emissions from the Global Scale

down to Point Sources Using Satellite Observations of Atmospheric Methane, Atmospheric Chemistry and Physics, 22, 9617–9646, https://doi.org/10.5194/acp-22-9617-2022, 2022.

Jervis, D., McKeever, J., Durak, B. O. A., Sloan, J. J., Gains, D., Varon, D. J., Ramier, A., Strupler, M., and Tarrant, E.: The GHGSat-D Imaging Spectrometer, Atmospheric Measurement Techniques, 14, 2127–2140, https://doi.org/10.5194/amt-14-2127-2021, 2021.

Jongaramrungruang, S., Frankenberg, C., Matheou, G., Thorpe, A. K., Thompson, D. R., Kuai, L., and Duren, R. M.: Towards Accurate Methane Point-Source Quantification from High-Resolution 2-D Plume Imagery, Atmospheric Measurement Techniques, 12, 6667–6681, https://doi.org/10.5194/amt-12-6667-2019, 2019.

Jongaramrungruang, S., Thorpe, A. K., Matheou, G., and Frankenberg, C.: MethaNet - An AI-driven Approach to Quantifying Methane Point-Source Emission from High-Resolution 2-D Plume Imagery, Remote Sensing of Environment, 269, 112 809, https://doi.org/10.1016/j.rse.2021.112809, 2022.

Joyce, P., Ruiz Villena, C., Huang, Y., Webb, A., Gloor, M., Wagner, F. H., Chipperfield, M. P., Barrio Guilló, R., Wilson, C., and Boesch, H.: Using a Deep Neural Network to Detect Methane Point Sources and Quantify Emissions from PRISMA Hyperspectral Satellite Images, Atmospheric Measurement Techniques, 16, 2627–2640, https://doi.org/10.5194/amt-16-2627-2023, 2023.

Krings, T., Gerilowski, K., Buchwitz, M., Reuter, M., Tretner, A., Erzinger, J., Heinze, D., Pflüger, U., Burrows, J. P., and Bovensmann, H.: MAMAP – a New Spectrometer System for Column-Averaged Methane and Carbon Dioxide Observations from Aircraft: Retrieval Algorithm and First Inversions for Point Source Emission Rates, Atmospheric Measurement Techniques, 4, 1735–1758, https://doi.org/10.5194/amt-4-1735-2011, 2011.

Kuhlmann, G., Broquet, G., Marshall, J., Clément, V., Löscher, A., Meijer, Y., and Brunner, D.: Detectability of CO_2 Emission Plumes of Cities and Power Plants with the Copernicus Anthropogenic CO_2 Monitoring (CO2M) Mission, Atmospheric Measurement Techniques, 12, 6695–6719, https://doi.org/10.5194/amt-12-6695-2019, 2019.

Kuhlmann, G., Brunner, D., Broquet, G., and Meijer, Y.: Quantifying CO2 Emissions of a City with the Copernicus Anthropogenic CO2 Monitoring Satellite Mission, Atmospheric Measurement Techniques, 13, 6733–6754, https://doi.org/10.5194/amt-13-6733-2020, 2020.

Liu, L., Chen, L., Liu, Y., Yang, D., Zhang, X., Lu, N., Ju, W., Jiang, F., Yin, Z., Liu, G., Tian, L., Hu, D., Mao, H., Liu, S., Zhang, J., Lei, L., Fan, M., Zhang, Y., Zhou, X., and Wu, Y.: Satellite Remote Sensing for Global Stocktaking: Methods, Progress and Perspectives, National Remote Sensing Bulletin, 26, 243–267, https://doi.org/10.11834/jrs.20221806, 2022.

Nassar, R., Hill, T. G., McLinden, C. A., Wunch, D., Jones, D. B. A., and Crisp, D.: Quantifying CO2 Emissions From Individual Power Plants From Space, Geophysical Research Letters, 44, 10 045–10 053, https://doi.org/10.1002/2017GL074702, 2017.

Nassar, R., Mastrogiacomo, J.-P., Bateman-Hemphill, W., McCracken, C., MacDonald, C. G., Hill, T., O'Dell, C. W., Kiel, M., and Crisp, D.: Advances in Quantifying Power Plant CO2 Emissions with OCO-2, Remote Sensing of Environment, 264, 112 579, https://doi.org/10.1016/j.rse.2021.112579, 2021.

Nisbet, E. G., Fisher, R. E., Lowry, D., France, J. L., Allen, G., Bakkaloglu, S., Broderick, T. J., Cain, M., Coleman, M., Fernandez, J., Forster, G., Griffiths, P. T., Iverach, C. P., Kelly, B. F. J., Manning, M. R., Nisbet-Jones, P. B. R., Pyle, J. A., Townsend-Small, A., al-Shalaan, A., Warwick, N., and Zazzeri, G.: Methane Mitigation: Methods to Reduce Emissions, on the Path to the Paris Agreement, Reviews of Geophysics, 58, e2019RG000 675, https://doi.org/10.1029/2019RG000675, 2020.

Nottrott, A., Kleissl, J., and Keeling, R.: Modeling Passive Scalar Dispersion in the Atmospheric Boundary Layer with WRF Large-Eddy Simulation, Atmospheric Environment, 82, 172–182, https://doi.org/10.1016/j.atmosenv.2013.10.026, 2014.

Özdemir, O. B. and Koz, A.: 3D-CNN and Autoencoder-Based Gas Detection in Hyperspectral Images, IEEE Journal of Selected Topics in Applied Earth Observations and Remote Sensing, 16, 1474–1482, https://doi.org/10.1109/JSTARS.2023.3235781, 2023.

Platt, N. and DeRiggi, D.: Comparative Investigation of Source Term Estimation Algorithms Using FUSION Field Trial 2007 Data: Linear Regression Analysis, International Journal of Environment and Pollution, 48, 13–21, https://doi.org/10.1504/IJEP.2012.049647, 2012.

Rodgers, C. D.: Inverse Methods for Atmospheric Sounding: Theory and Practice, vol. 2 of *Series on Atmospheric, Oceanic and Planetary Physics*, WORLD SCIENTIFIC, https://doi.org/10.1142/3171, 2000.

Sánchez-García, E., Gorroño, J., Irakulis-Loitxate, I., Varon, D. J., and Guanter, L.: Mapping Methane Plumes at Very High Spatial Resolution with the WorldView-3 Satellite, Atmospheric Measurement Techniques, 15, 1657–1674, https://doi.org/10.5194/amt-15-1657-2022, 2022.

Stockie, J. M.: The Mathematics of Atmospheric Dispersion Modeling, Siam Review, 53, 349–372, https://doi.org/10.1137/10080991X, 2011.

Stoll, R., Gibbs, J. A., Salesky, S. T., Anderson, W., and Calaf, M.: Large-Eddy Simulation of the Atmospheric Boundary Layer, Boundary-Layer Meteorology, 177, 541–581, https://doi.org/10.1007/s10546-020-00556-3, 2020.

Storn, R. and Price, K.: Differential Evolution - A Simple and Efficient Heuristic for Global Optimization over Continuous Spaces, Journal of Global Optimization, 11, 341–359, https://doi.org/10.1023/A:1008202821328, 1997.

Suarez, D. R., Rozendaal, D. M. A., De Sy, V., Phillips, O. L., Alvarez-Davila, E., Anderson-Teixeira, K., Araujo-Murakami, A., Arroyo, L., Baker, T. R., Bongers, F., Brienen, R. J. W., Carter, S., Cook-Patton, S. C., Feldpausch, T. R., Griscom, B. W., Harris, N., Herault, B., Honorio Coronado, E. N., Leavitt, S. M., Lewis, S. L., Marimon, B. S., Monteagudo Mendoza, A., N'dja, J. K., N'Guessan, A. E., Poorter, L., Qie, L., Rutishauser, E., Sist, P., Sonke, B., Sullivan, M. J. P., Vilanova, E., Wang, M. M. H., Martius, C., and Herold, M.: Estimating Aboveground Net Biomass Change for Tropical and Subtropical Forests: Refinement of IPCC Default Rates Using Forest Plot Data, Global Change Biology, 25, 3609–3624, https://doi.org/10.1111/gcb.14767, 2019.

Sutton, O. G.: A Theory of Eddy Diffusion in the Atmosphere, Proceedings of the Royal Society of London, Series A,, 135, 143–165, 1932.

Thorpe, A. K., Frankenberg, C., and Roberts, D. A.: Retrieval Techniques for Airborne Imaging of Methane Concentrations Using High Spatial and Moderate Spectral Resolution: Application to AVIRIS, Atmospheric Measurement Techniques, 7, 491–506, https://doi.org/10.5194/amt-7-491-2014, 2014.

Varon, D. J., Jacob, D. J., McKeever, J., Jervis, D., Durak, B. O. A., Xia, Y., and Huang, Y.: Quantifying Methane Point Sources from Fine-Scale Satellite Observations of Atmospheric Methane Plumes, Atmospheric Measurement Techniques, 11, 5673–5686, https://doi.org/10.5194/amt-11-5673-2018, 2018.

Xu, J., Ma, Z., Yan, S., and Peng, J.: Do ERA5 and ERA5-land Precipitation Estimates Outperform Satellite-Based Precipitation Products? A Comprehensive Comparison between State-of-the-Art Model-Based and Satellite-Based Precipitation Products over Mainland China, Journal of Hydrology, 605, 127 353, https://doi.org/10.1016/j.jhydrol.2021.127353, 2022.

Yang, D., Hakkarainen, J., Liu, Y., Ialongo, I., Cai, Z., and Tamminen, J.: Detection of Anthropogenic CO2 Emission Signatures with TanSat CO2 and with Copernicus Sentinel-5 Precursor (S5P) NO2 Measurements: First Results, Advances in Atmospheric Sciences, 40, 1–5, https://doi.org/10.1007/s00376-022-2237-5, 2023.

Zhang, Y., Gautam, R., Pandey, S., Omara, M., Maasakkers, J. D., Sadavarte, P., Lyon, D., Nesser, H., Sulprizio, M. P., Varon, D. J., Zhang, R., Houweling, S., Zavala-Araiza, D., Alvarez, R. A., Lorente, A., Hamburg, S. P., Aben, I., and Jacob, D. J.: Quantifying Methane Emissions from the Largest Oil-Producing Basin in the United States from Space, Science Advances, 6, eaaz5120, https://doi.org/10.1126/sciadv.aaz5120, 2020.

Zhao, Y., Zhou, Y., Qiu, L., and Zhang, J.: Quantifying the Uncertainties of China's Emission Inventory for Industrial Sources: From National to Provincial and City Scales, Atmospheric Environment, 165, 207–221, https://doi.org/10.1016/j.atmosenv.2017.06.045, 2017.